

# Active Control of Adaptive Optics System in a Large Segmented Mirror Telescope

M. Nagashima and B. N. Agrawal

## Abstract

For a large Adaptive Optics (AO) system such as a large Segmented Mirror Telescope (SMT), it is often difficult, although not impossible, to directly apply common Multi-Input Multi-Output (MIMO) controller design methods due to the computational burden imposed by the large dimension of the system model. In this paper, a practical controller design method is proposed which significantly reduces the system dimension for a system where the dimension required to represent the dynamics of the plant is much smaller than the dimension of the full plant model. The proposed method decouples the dynamic and static parts of the plant model by a modal decomposition technique to separately design a controller for each part. Two controllers are then combined using so-called Sensitivity Decoupling Method (SDM) so that the resulting feedback loop becomes the superposition of the two individual feedback loops of the dynamic and static parts. A MIMO controller was designed by the proposed method using the  $H_\infty$  loop shaping technique for an SMT model to be compared with other controllers proposed in the literature. Frequency-domain analysis and time-domain simulation results show the superior performance of the proposed controller.

Keywords: word; Segmented Mirror Telescope, adaptive optics, H-infinity control, modal decomposition, Sensitivity Decoupling Method

## I INTRODUCTION

In optical systems used for imagery, such as telescopes for astronomy or surveillance of the earth surface from the space, the diameter of the lens determines the maximum angular resolution of the acquired image, i.e., the larger the telescope diameter, the higher the possible resolution of the image. For telescopes in the space, on the other hand, launching a large solid optical mirror is very challenging and also expensive. Hubble Space Telescope has a primary mirror of 2.4 m diameter, but it is difficult to further extend the size of the mirror because no launch vehicle is available for such a large object. To overcome this problem, so-called Segmented Mirror Telescope (SMT) has been developed, which has several smaller size mirrors to form one large mirror surface instead of a single monolithic mirror. One of the challenges for an SMT is the phase aberration caused by the vibration of the mirror structure which introduces distortions in the final image.

Adaptive Optics (AO) refers to an optical control system where the phase aberration of the incoming light is measured by a wavefront sensor (WFS) and corrected by a Deformable Mirror (DM) which has the capability of changing the phase of the reflected light by the deformation of the mirror surface (Tyson, 2010). For static aberration caused by imperfection, misalignment, and/or deformation of the optical components due to the gravity or other causes, the phase correction can be done in an open-loop manner. For time varying aberrations, such as atmospheric aberration or vibration of the structure, a feedback control is usually necessary. Rather simple classical Proportional-Integral-Derivative (PID) type feedback control had traditionally been used as a primary control law in AO, but more advanced control schemes, such as optimal control (Gavel and Wiberg, 2003; Le Roux et al., 2004; Petit et al., 2006) or adaptive control (Rhoadarmer, Klein, Gibson, Chen and Liu, 2006; Liu and Gibson, 2007) have been proposed in recent years.

In conventional AO, the dynamics of the plant, that is the path from the deformable mirror input to the wavefront sensor output, has been ignored assuming that the response of the DM is fast enough compared to the sample rate of the sensor. Only the static coupling of the input and output channels and a pure time delay introduced by the hardware have been considered in the controller design. In SMTs, however, the segment mirrors constituting the deformable mirror are rather flexible due to the large size and the light weight material used to reduce the launching cost. The dynamics of the deformable mirror can no longer be ignored and need to be taken into account in the controller design.

From control point of view, the AO system of an SMT is a large Multi-Input Multi-Output (MIMO) system with hundreds or even thousands of input and output channels. The dimension of the model is often prohibitively large for direct application of popular MIMO controller design techniques. For example, a three-meter Segment Mirror Telescope with six segment mirrors can have more than 900 actuator input and 700 sensor output and 300 states (Burtz, 2009). A plant model with such a dimension is too large for numerical tools readily available for MIMO controller design. Even if the computation is somehow carried out, the resulting controller will have an impractically large dimension to be implemented and operated in real-time.

Recently, Burtz (2009) and Looyesen (2009) worked on the controller design for a three meter SMT using modal decomposition techniques. Modal decomposition projects the observed error onto a set of basis vectors and it has some advantages such as reducing the noise effect and computational expense. Zernike polynomial had been commonly used to form a set of modes, or a basis, in AO (Allen, 2007; Allen, Kim and Agrawal, 2008), but other modes have been proposed recently such as Singular Value Decomposition (SVD) modes (Gibson, Chang and Chen, 2001), Frequency-Weighted modes (Liu and Gibson, 2007; Monirabbasi and Gibson, 2010), Fourier modes (Poyneer, Macintosh and Véran, 2007; Nagashima and Agrawal, 2011), and wavelet (Hampton, Agathoklis, Conan and Bradley, 2010).

Burtz proposed controllers designed by the  $H_\infty$  loop shaping where Zernike polynomial and SVD modes were used to reduce the dimension of the model. The first 21 modes from the lowest order, excluding the piston mode, were selected out of 720 modes for the Zernike basis and the 21 modes associated with the largest singular values of the poke matrix were selected for the SVD basis. The number of states of the plant was also reduced by the Hankel singular value reduction technique. Looyesen proposed a controller which combines the  $H_\infty$  controller proposed by Burtz in parallel with a classical controller. The classical controller is an integrator combined in series with a comb filter or an elliptic low pass filter to attenuate the plant resonances for stability.

One of the shortcomings of these methods is that the controller only addresses the disturbance that is projected onto the selected modes, or basis vectors, and the part of the disturbance that are orthogonal to those basis vectors are ignored. The performance can be improved by increasing the number of modes to be included, but the required computation also increases with the number of modes. Selecting a basis with which the disturbance energy is concentrated on a small number of modes can improve the performance without increasing the computational burden, but it is only possible when the disturbance spatial characteristics are known *a priori*. While a controller with a large dimension simply cannot be avoided for a plant which contains a large number of states that are fully coupled, there is a class of plant in which significant part of the plant dimension is related to the static behaviour of the plant and the dynamics of the plant can be represented with a smaller dimension without any approximation. For such a plant, it is possible to design a controller which addresses all static and dynamic modes without computational difficulties.

In this paper, a practical controller design method is proposed for a class of plant where the dynamic part of the plant can be separated from the static part through modal decomposition technique to obtain an equivalent smaller dimension model for controller design. Controllers for dynamic and static parts are designed separately and then combined using so-called Sensitivity Decoupling Method (SDM) (Mori, Munemoto, Otsuki, Yamaguchi and Akagi, 1991). The resulting smaller dimension controller does not ignore any mode and the performance is not sacrificed for the sake of computation. Three other controllers, namely, a conventional integral controller, a MIMO controller based on Burtz (2009), and a parallel controller based on Looyen (2009) are also designed to compare the performances with the proposed controller.

In the next section, a summary of conventional AO control is presented from control perspective. Section III presents the plant model considered in this paper and the four controllers designed for this plant. Frequency domain analysis of each controller is presented in this section and the time domain simulation results are given in Section IV, followed by the conclusion in Section V.

## II ADAPTIVE OPTICS CONTROL

A typical AO feedback control system shown in Figure 1 consists of three primary components, a wavefront sensor to detect the phase aberration, a deformable mirror (DM) to correct the detected aberration, and a control computer to calculate the command for the DM. A beam with a known phase called reference beam is usually used as a reference against which the aberration introduced in the optical path is measured. Shack-Hartmann (SH) wavefront sensor (WFS) is one of the common wavefront sensors used in AO systems. Figure 2 shows the schematic of a typical SH sensor. It measures the local gradients of the phase by an array of lenslets which produces a grid pattern of bright spots on a CCD or CMOS camera located at the focal length of the lenslets. The grid pattern is compared with the grid pattern obtained from a reference beam and the  $x$  and  $y$  deviations of the spots are measured. The deviation is proportional to the gradient, or the slope, of the phase at the measured grid, which can be computed by the following formula (Tyson and Frazier, 2004).

$$\theta_x = \frac{\delta_x}{f}, \quad \theta_y = \frac{\delta_y}{f} \quad (1)$$

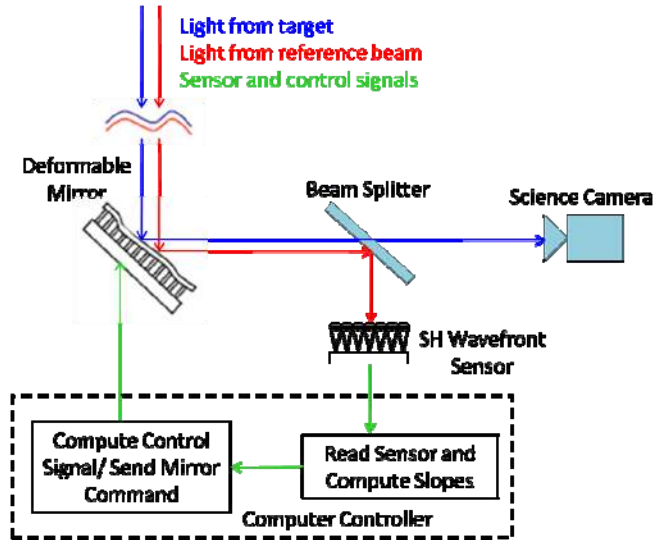


Figure 1 Typical adaptive optics system with Shack-Hartmann wavefront sensor

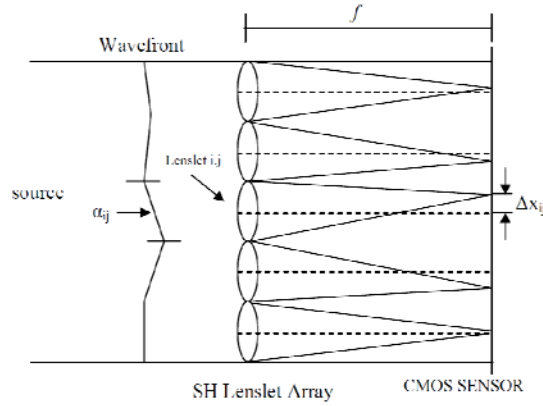


Figure 2 Shack-Hartmann wavefront sensor schematic [From (Allen, 2007)]

Here,  $\theta_x$  and  $\theta_y$  are the slope angles in radians,  $\delta_x$  and  $\delta_y$  are the deviation of the spot centre from the reference spot centre in  $x$  and  $y$  direction, and  $f$  is the focal length of the lenslets. The spot centre, sometimes called the centroid, is computed by the following formula,

$$P_x = \frac{\sum_{i=1}^N x_i m_i}{\sum_{i=1}^N m_i}, \quad P_y = \frac{\sum_{i=1}^N y_i m_i}{\sum_{i=1}^N m_i}, \quad (2)$$

where,  $(P_x, P_y)$  represents the coordinate of the spot centre,  $m_i$  is the intensity of the pixel located at  $(x_i, y_i)$ , and  $N$  is the number of the pixels in the grid.

## II-1 Feedback Control of Adaptive Optics System

The system in Figure 1 can be represented by an equivalent diagram from control point of view as shown in Figure 3. The actuator command is represented by a vector  $\mathbf{u}(k)$  and the sensor output is represented by a vector  $\mathbf{y}(k)$ . These vectors form two vector spaces called the actuator space and sensor space. The dimensions of the actuator space and the sensor space are the number of the actuator channels and that of the sensor channels, respectively. For SH WFS, the output is the  $x$  and  $y$  component of the phase gradient and thus the number of the channels is twice the number of the lenslets. The disturbance is represented by a vector  $\varphi$  defined in the sensor space, i.e., the disturbance observed by the wavefront sensor. Since the disturbance represents a phase that varies with time, it has spatial and temporal frequency components. The measurement noise  $\mathbf{v}$  represents any error introduced in the measurement. In AO, the reference is usually zero, i.e., a flat wavefront and the error vector  $\mathbf{e}(k)$  is defined in the sensor space. The delay in the system is separated from the dynamics of the plant and represented by a pure time delay  $z^{-q}$ .

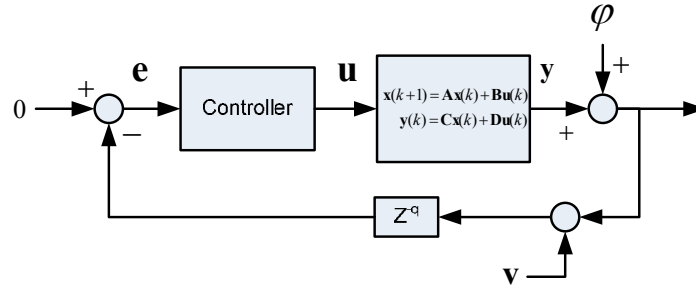


Figure 3 Diagram of adaptive optics system from control perspective

The path from  $\mathbf{u}(k)$  to  $\mathbf{y}(k)$  is a Multi-Input Multi-Output (MIMO) plant which can be represented by the following standard discrete-time state-space model.

$$\begin{aligned} \mathbf{x}(k+1) &= \mathbf{A}\mathbf{x}(k) + \mathbf{B}\mathbf{u}(k) \\ \mathbf{y}(k) &= \mathbf{C}\mathbf{x}(k) + \mathbf{D}\mathbf{u}(k) \end{aligned} \quad (3)$$

For a small scale AO where the DM dynamics can be ignored, the plant is often approximated by a constant matrix  $\mathbf{\Gamma}$  called poke matrix or influence matrix. The poke matrix is the steady state response of the plant to a unit step input which can be written as

$$\mathbf{\Gamma} = \mathbf{C}(\mathbf{I} - \mathbf{A})^{-1}\mathbf{B} + \mathbf{D}. \quad (4)$$

For AO systems involving larger flexible structures such as SMTs, the dynamics of the system can no longer be ignored. But the poke matrix still provides useful information on the steady state coupling of the input and output channels. For an AO system approximated by a poke matrix, one of the common approaches is to use modal decomposition techniques to convert the observed error to a set of coefficients of the chosen modes and apply a control law in this new vector space referred to as the control space or the coefficient space. One of the advantages of this approach is it can uncouple

the input and output channels of the plant in the control space, which is equivalent of diagonalizing the poke matrix. Once uncoupled, an SISO controller can be applied to the uncoupled channels.

For a system where the dynamics can be ignored except for the step delay, an integral controller can provide a sufficient performance for a class of disturbance which has a simple low-pass temporal frequency spectrum. Due to the absence of dynamics in the plant, the stability boundary of the feedback loop gain is usually high enough to achieve the desired bandwidth. The practical upper bound of the gain is likely determined by the actuator capability and/or the level of the measurement noise in the system. For a disturbance with more complex temporal frequency spectrum, a higher order SISO controller can be applied to achieve better performance.

## II-2 Modal Decomposition

Figure 4 shows the diagram of a controller that applies a control law in the control space. The row vectors of the matrix  $\mathbf{F}$  are the modes onto which the observed error is projected and  $\mathbf{G}$  is the matrix that converts the controller output to the actuator space. For an  $m \times n$  poke matrix  $\mathbf{\Gamma}$  with rank  $r$ , an  $r \times m$  matrix  $\mathbf{F}$  and  $\mathbf{G} = (\mathbf{F}\mathbf{\Gamma})^\dagger$  can uncouple  $\mathbf{\Gamma}$  provided that the row vectors of  $\mathbf{F}$  are linearly independent to form a basis that spans the column vector space of  $\mathbf{\Gamma}$ . Here,  $\dagger$  denotes the pseudo inverse defined as

$$\mathbf{A}^\dagger = \mathbf{A}^T (\mathbf{A}\mathbf{A}^T)^{-1} \quad (5)$$

for an  $r \times n$  matrix  $\mathbf{A}$  whose rank is  $r$  and  $r < n$ . The path from  $\mathbf{u}_c$  to  $\mathbf{e}_c$  along the feedback loop is uncoupled by  $\mathbf{F}$  and  $\mathbf{G}$  as follows.

$$\mathbf{F}\mathbf{\Gamma}\mathbf{G} = \mathbf{F}\mathbf{\Gamma}(\mathbf{F}\mathbf{\Gamma})^\dagger = \mathbf{I} \quad (6)$$

Here,  $\mathbf{I}$  is an  $r \times r$  identity matrix. If  $m > n$  and  $\mathbf{\Gamma}$  has the full rank  $n$ , then  $\mathbf{F}$  can simply be the following pseudo inverse of  $\mathbf{\Gamma}$  defined differently from Equation (5) as follows.

$$\mathbf{\Gamma}^\dagger = (\mathbf{\Gamma}^T\mathbf{\Gamma})^{-1}\mathbf{\Gamma}^T \quad (7)$$

The corresponding matrix  $\mathbf{G}$  is an identity matrix in this case.

The basis for the control space, i.e., the row vectors of  $\mathbf{F}$ , can be any set of vectors as long as they span the sensor space that can be influenced by the actuator. Zernike polynomial is often used as the basis in AO, since it has convenient properties for circular apertures and has been well-studied. In case of SMT, however, the phase aberration is expected to be caused by the vibration of the segment mirrors which is highly localized at each segment. Zernike basis is not necessarily a good choice for this type of disturbance, and the basis used in this paper is obtained by applying the Singular Value Decomposition (SVD) to the poke matrix. One of the advantages of the SVD basis is that it is orthogonal and guaranteed to span the column vector space of the poke matrix since the basis is derived from it. Another advantage is that the basis vectors are ordered by the magnitudes of the associated singular values which can be viewed as the gain of the plant to influence those modes.

SVD is defined as

$$\mathbf{\Gamma} = \mathbf{U}\mathbf{\Sigma}\mathbf{V}^T, \quad (8)$$

where,  $\mathbf{U}$  and  $\mathbf{V}$  are matrices whose column vectors are orthogonal and normalized. For  $m \times n$  matrix  $\mathbf{\Gamma}$ , the size of  $\mathbf{U}$  and  $\mathbf{V}$  are  $m \times m$  and  $n \times n$ , respectively. The matrix  $\mathbf{\Sigma}$  is an  $m \times n$  diagonal matrix whose diagonal components are the singular values of the matrix  $\mathbf{\Gamma}$ . If the rank of  $\mathbf{\Gamma}$  is  $r < \min\{m, n\}$ , only the first  $r$  diagonal components of  $\mathbf{\Sigma}$  have non-zero values and  $\mathbf{\Sigma}$  can be reduced to an  $r \times r$  matrix with  $\mathbf{U}$  and  $\mathbf{V}$  correspondingly reduced to have only the first  $r$  columns. The poke matrix can be diagonalized by the matrices  $\mathbf{U}$  and  $\mathbf{V}$  as follows.

$$\mathbf{U}^T \mathbf{\Gamma} \mathbf{V} = \mathbf{U}^T \mathbf{U} \mathbf{\Sigma} \mathbf{V}^T \mathbf{V} = \mathbf{\Sigma} \quad (9)$$

The size of diagonal matrix can be arbitrarily reduced below the rank of  $\mathbf{\Gamma}$  by reducing the number of columns in  $\mathbf{U}$  and  $\mathbf{V}$ . Let  $\mathbf{U}_l$  and  $\mathbf{V}_l$  be matrices consisting of the first  $l < r$  columns of  $\mathbf{U}$  and  $\mathbf{V}$ , respectively. Then,

$$\mathbf{U}_l^T \mathbf{\Gamma} \mathbf{V}_l = \mathbf{\Sigma}_l, \quad (10)$$

where  $\mathbf{\Sigma}_l$  is a  $l \times l$  diagonal matrix containing the first  $l$  singular values of  $\mathbf{\Sigma}$ . For  $l \leq r$ ,  $\mathbf{\Sigma}_l$  is invertible, and pre-multiplying the inverse of  $\mathbf{\Sigma}_l$  with  $\mathbf{V}_l$  yields a normalized diagonal matrix, i.e., an  $l \times l$  identity matrix. Therefore, choosing

$$\mathbf{F} = \mathbf{U}_l^T, \quad \mathbf{G} = \mathbf{V}_l \mathbf{\Sigma}_l^{-1} \quad (11)$$

will uncouple and normalize the feedback path from  $\mathbf{u}_c$  to  $\mathbf{e}_c$  in Figure 4 as follows.

$$\mathbf{e}_c = 0 - \mathbf{F} \mathbf{\Gamma} \mathbf{G} \mathbf{u}_c = -(\mathbf{U}_l^T) \mathbf{\Gamma} (\mathbf{V}_l \mathbf{\Sigma}_l^{-1}) \mathbf{u}_c = -\mathbf{u}_c \quad (12)$$

### III CONTROLLER DESIGN

In this section, the plant model considered in this paper is presented and four controllers, namely, an integral controller, an  $H_\infty$  controller, a parallel controller, and the proposed dynamics decoupling controller are designed for the plant. The singular value plots of the controllers are presented to show the characteristics of each control scheme in the frequency domain.

#### III-1 Plant Model

Figure 5 shows an example of the type of SMTs considered here. It has a Cassegrain configuration where the incoming light is reflected by the primary mirror to the secondary mirror which in turn reflects the light back through the hole in the center to the optical sensors on the back.

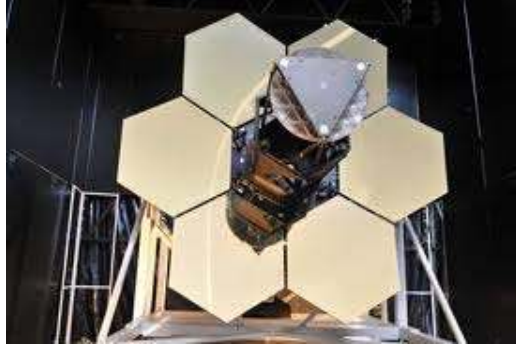


**Figure 5 Segmented Mirror Telescope at Naval Postgraduate School**

The segmented primary mirror is constituted by six hexagonal segment mirrors and functions as one large discontinuous surface mirror, while each segment is a continuous surface mirror actuated by an array of Piezo-electric (PZT) actuators placed on the back of the mirror structure. The SMT model considered in this study can be written in the following state-space form, where  $\mathbf{u}(k) \in \mathfrak{R}^n$  is the actuator command and  $\mathbf{y}(k) \in \mathfrak{R}^m$  is the wavefront sensor output. The step delay in the feedback loop is treated separately from the plant model.

$$\begin{aligned}\mathbf{x}(k+1) &= \mathbf{A}_{AO}\mathbf{x}(k) + \mathbf{B}_{AO}\mathbf{u}(k) \\ \mathbf{y}(k) &= \mathbf{C}_{AO}\mathbf{x}(k) + \mathbf{D}_{AO}\mathbf{u}(k)\end{aligned}\tag{13}$$

The dimension of the input  $n$  is 936 and output  $m$  is 720, and the number of the states  $l$  is 332. The dimension of the  $\mathbf{A}_{AO}$ ,  $\mathbf{B}_{AO}$ ,  $\mathbf{C}_{AO}$ , and  $\mathbf{D}_{AO}$  are therefore  $[332 \times 332]$ ,  $[332 \times 936]$ ,  $[720 \times 332]$ , and  $[720 \times 936]$ , respectively. The sample rate of the model  $T_s$  is 2000 Hz. Figure 6 shows the frequency spectra of the 116 second order modes represented by the  $\mathbf{A}_{AO}$  matrix whose natural frequencies range from 30 Hz to 770 Hz. Figure 7 shows the singular value plot of the plant. Compared with the segmented space telescope model investigated in (Li, Kosmatopoulos, Ioannou and Ryaciotaki-Boussalis, 2000) and (Whorton, 2003) and the AO systems in (Frazier, 2003) where the number of the Input-Output (IO) channels range from 18 to 162 and the number of the states range from 70 to 200, the model has significantly larger dimension and it is difficult to take the same approach to design the controller.

One of the unique properties of this particular SMT model is that while  $\mathbf{D}_{AO}$  has a full rank of 720, the rank of  $\mathbf{B}_{AO}$  is only 102 and it is contributing much less to the overall degree of freedom of the system. The matrix  $\mathbf{D}_{AO}$  can be considered as a poke matrix that represents the "static" behaviour of the plant, and the column vectors of  $\mathbf{B}_{AO}$  represent the spatial modes that excite the dynamics of the plant. The insufficient rank of  $\mathbf{B}_{AO}$  indicates that the dimension of the actuator subspace that can excite the plant dynamics is much smaller than the dimension of the whole actuator space. This property is exploited for reduction of the model in the proposed method which will be shown in section III-5. For this plant, the desired bandwidth is set to 10Hz.



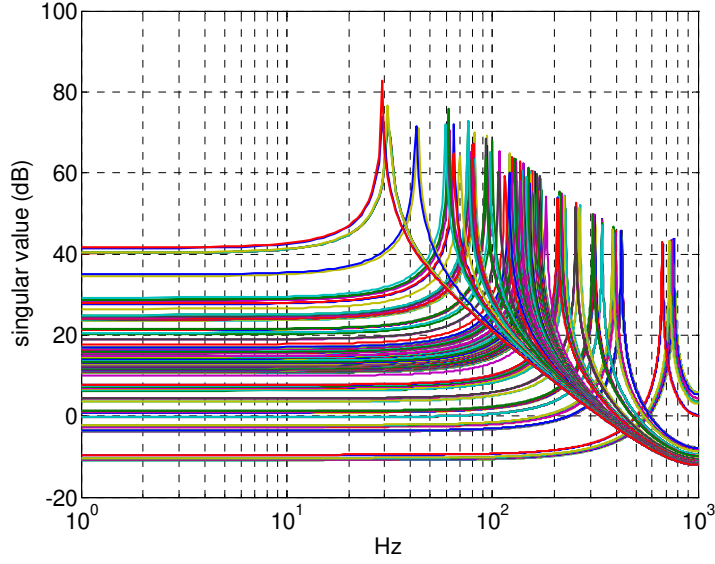


**Figure 6 Frequency spectra of the second order modes of the plant**

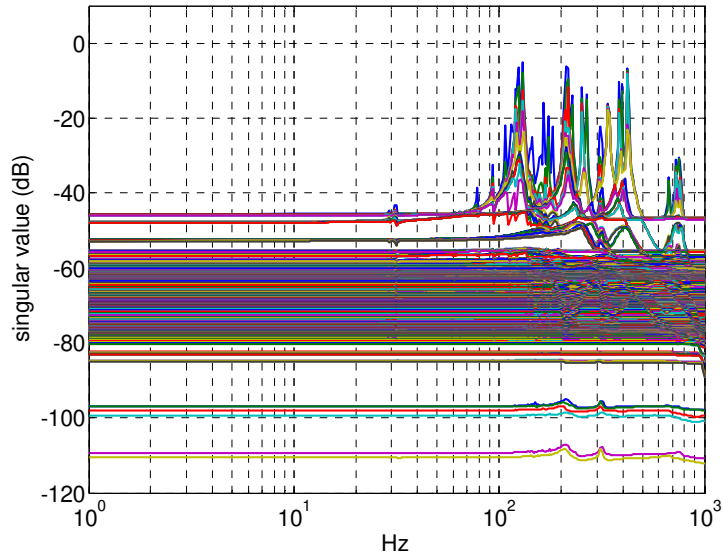


**Figure 7 Singular value plot of the plant**

### III-2 Integral Controller

The poke matrix of the SMT plant and its SVD are written as follows.

$$\Gamma_{AO} = \mathbf{C}_{AO}(\mathbf{I} - \mathbf{A}_{AO})^{-1}\mathbf{B}_{AO} + \mathbf{D}_{AO} = \mathbf{U}_{AO}\mathbf{\Sigma}_{AO}\mathbf{V}_{AO}^T \quad (14)$$

The poke matrix has a full rank of 720 and the dimension of  $\mathbf{U}_{AO}$ ,  $\mathbf{\Sigma}_{AO}$ , and  $\mathbf{V}_{AO}$  are  $[720 \times 720]$ ,  $[720 \times 720]$ , and  $[936 \times 720]$ , respectively. The plant transfer function matrix is written as

$$\mathbf{P}(z) = \mathbf{C}_{AO}(\mathbf{I}z - \mathbf{A}_{AO})^{-1}\mathbf{B}_{AO} + \mathbf{D}_{AO} \quad (15)$$

and the plant in the control space is written as

$$\mathbf{P}_c(z) = \mathbf{U}_{AO}^T \mathbf{P}(z) \mathbf{V}_{AO} \boldsymbol{\Sigma}_{AO}^{-1}. \quad (16)$$

The plant dimension is reduced from  $[720 \times 936]$  to  $[720 \times 720]$ , but only the redundancy of the actuator is removed and the entire sensor space can still be controlled. Figure 8 shows the singular value plot of  $\mathbf{P}_c(z)$ . It can be seen that the singular values of the new plant  $\mathbf{P}_c(z)$  is normalized by the value at the lowest frequency.

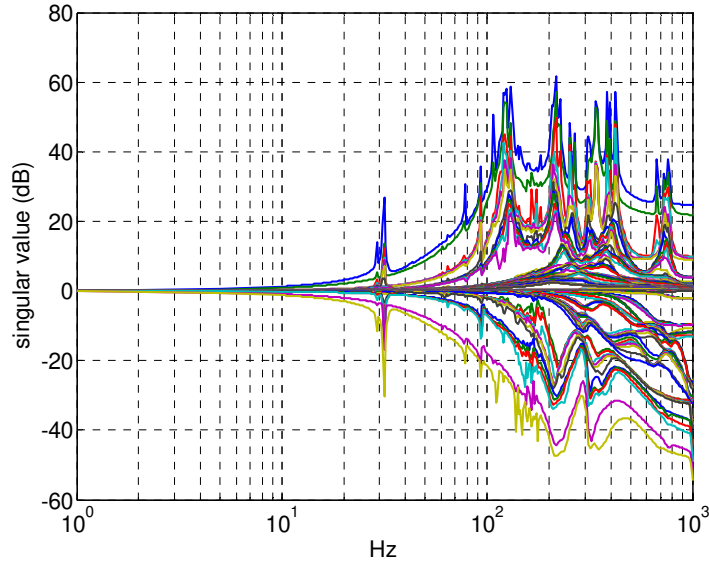


**Figure 8 Singular value plot of the plant in control space**

For static disturbance, the simplest controller to eliminate steady state error is an integral controller applied to all statically uncoupled channels. Let this integral controller be

$$f_i(z) = K_i \frac{z}{z-1}. \quad (17)$$

Then, the actual controller that takes the sensor output and produces the actuator command is written as

$$\mathbf{C}_i(z) = \mathbf{V}_{AO} \boldsymbol{\Sigma}_{AO}^{-1} [f_i(z) \mathbf{I}] \mathbf{U}_{AO}^T. \quad (18)$$

Here,  $\mathbf{I}$  is an identity matrix of  $[720 \times 720]$  and a constant  $K_i$  is used for all channels since all channels are approximately normalized for the frequencies of interest below the first resonance around 30 Hz. The open-loop transfer function matrix  $\mathbf{L}_i(z)$ , the complementary sensitivity function matrix  $\mathbf{T}_i(z)$ , and the sensitivity function matrix  $\mathbf{S}_i(z)$  for this controller are written as follows.

$$\mathbf{L}_i(z) = z^{-1}\mathbf{P}(z)\mathbf{C}_i(z) \quad (19)$$

$$\mathbf{T}_i(z) = \mathbf{L}_i(z)[1 + \mathbf{L}_i(z)]^{-1} \quad (20)$$

$$\mathbf{S}_i(z) = [1 + \mathbf{L}_i(z)]^{-1} \quad (21)$$

The singular values of the  $\mathbf{C}_i(z)$  has a simple low-pass spectrum and it can be shown that there exists  $K_i$  that is small enough to make the feedback system stable by sufficiently attenuating the open-loop gain at high frequencies where the coupling effect becomes significant and the pole matrix approximation does not hold.

Figure 9 is the plot of the open-loop singular values for  $K_i = 0.0022$  which is near the stability boundary. Figure 10 and Figure 11 are the singular value plots of the complementary sensitivity function and sensitivity function matrices, respectively. The closed-loop 3dB bandwidth is less than 1 Hz, which is much lower than the desired 10Hz bandwidth. This approach is very robust, but the resulting controller tends to be too conservative.

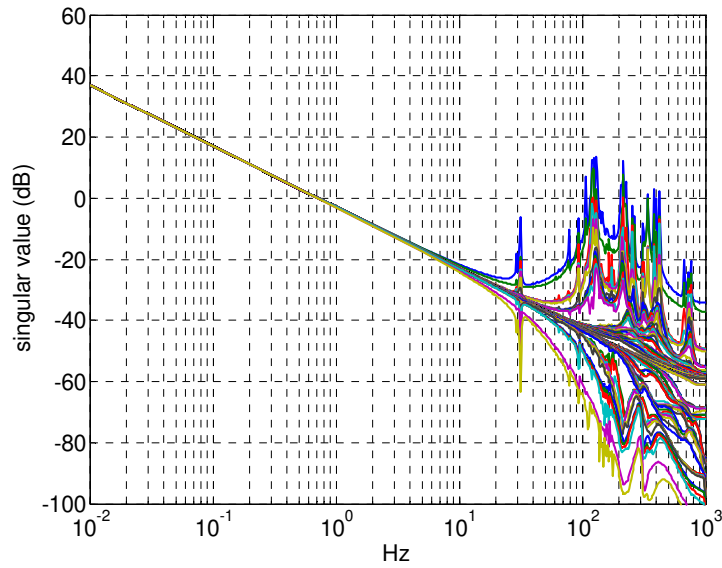


**Figure 9 Singular value plot of the open-loop function of the integral controller in sensor space**

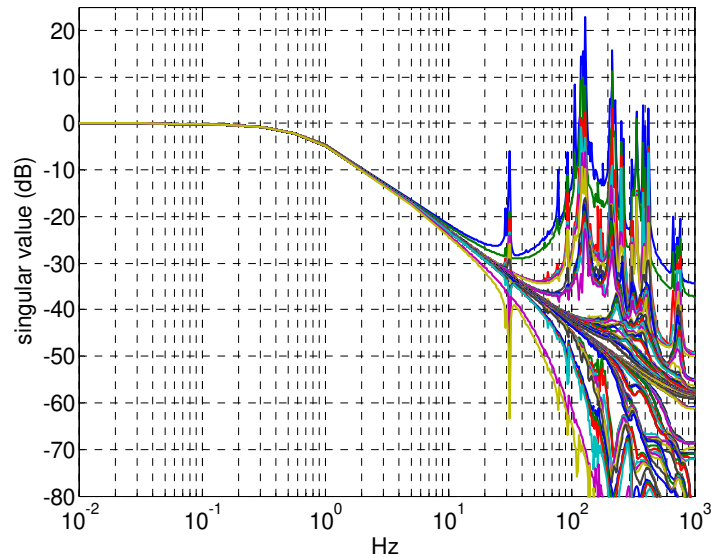


**Figure 10 Singular value plot of the complementary sensitivity function of the integral controller in sensor space**

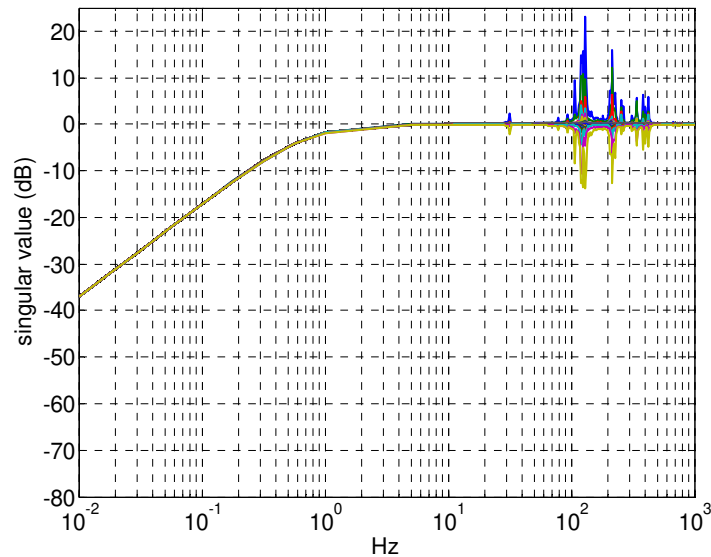


**Figure 11 Singular value plot of the sensitivity function of the integral controller in sensor space**

### III-3 $H_\infty$ Controller Design

The performance of the integral controller given in the previous section is very limited since it does not fully exercise the degree of freedom of the plant. A true MIMO controller can be applied to improve the performance, and there are several numerical methods available to design a MIMO controller for a given plant. One of the common methods is the  $H_\infty$  mixed sensitivity loop shaping, which aims to obtain a stable controller that satisfies the design requirements specified as the shape of the singular values of the transfer function matrices, such as the sensitivity function or

complementary sensitivity function. This design method, however, requires extensive computation and the computational burden increases significantly as the dimension of the plant increases. Although it is still possible to carry out the computation, the resulting controller aiming to address all channels and all controllable states of the plant can be very large and impractical to be implemented. For this reason, the input and output channels were reduced in (Burtz, 2009) through modal decomposition described in Section II to make the model tractable for the  $H_\infty$  mixed sensitivity loop shaping. In this approach, the selection of the basis modes to be addressed by the controller is critical and the performance of the controller depends on the spatial characteristics of the disturbance and the selected basis modes.

To illustrate this point, an  $H_\infty$  controller is designed in this section. The controller assumes a particular disturbance profile and SVD basis modes are chosen so that the maximum attenuation can be achieved with the limited number of modes. The disturbance used here is the response of the plant observed in the steady state when unit input was applied to all actuator channels. The disturbance observed in the sensor space is equivalent of the sum of all column vectors of the poke matrix and Figure 12 shows the projection of this disturbance onto the column vectors of  $\mathbf{U}_{AO}$ .

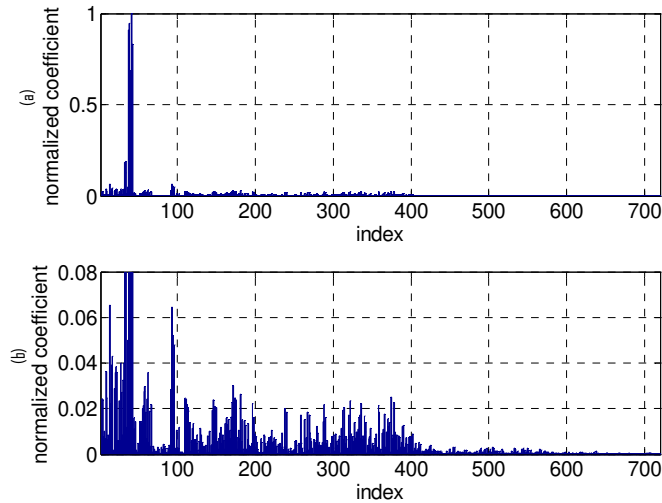


**Figure 12 Projection of the disturbance on the SVD basis: (a) normal view, (b) magnified view**

The upper plot (a) shows the coefficients in full scale and the lower plot (b) shows the magnified view. It can be seen that distribution is not uniform but with some concentration on certain modes. In order to make the basis vector selection process easier, the basis vectors is sorted according to the magnitude of the projected disturbance. It can be obtained by post-multiplying the permutation matrix  $\mathbf{M}$  representing the sorting order to the original basis vector matrix as follows.

$$\mathbf{U}_H = \mathbf{U}_{AO}\mathbf{M}, \quad \mathbf{V}_H = \mathbf{V}_{AO}\mathbf{M}, \quad \mathbf{\Sigma}_H = \mathbf{\Sigma}_{AO}\mathbf{M}. \quad (22)$$

The subscript H indicates the column vectors of the matrix are sorted. Figure 13 shows the projection of the disturbance on the sorted vectors.

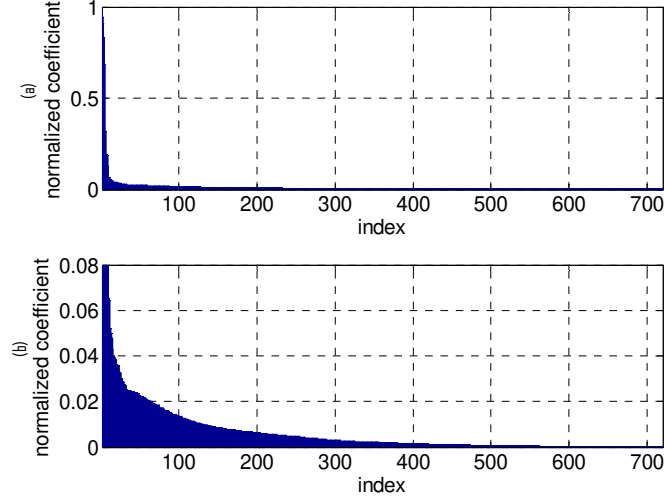


**Figure 13 Projection of the disturbance on the sorted SVD basis: (a) normal view, (b) magnified**

The basis vectors can now be selected by setting a threshold for the projected values to cut off the modes or by specifying the number of modes to be controlled. The number of the modes to be addressed by the  $H_\infty$  controller is decided to be 102 and the reduced plant can be written as follows with  $\mathbf{U}_H$ ,  $\mathbf{V}_H$ , and  $\mathbf{\Sigma}_H^{-1}$  whose number of columns are reduced to 102.

$$\mathbf{P}_H(z) = \mathbf{U}_H^T \mathbf{P}(z) \mathbf{V}_H \mathbf{\Sigma}_H^{-1} \quad (23)$$

Notice that this disturbance is just an example and it does not reflect the actual disturbance expected to be observed by the SMT. It is used here to simply demonstrate the case where the disturbance spatial characteristics are known. In addition to the input and output channel reduction, the state of the model can also be reduced using the Hankel singular value reduction technique presented in (Burtz, 2009; Looysen, 2009). In this paper, however, the state reduction is not applied in order to make a fair performance comparison with the proposed controller which does not require state reduction.

Once the modal reduction is complete, the discrete-time  $H_\infty$  mixed sensitivity loop shaping problem can be formulated as follows. Given the desired shapes of the singular values of the sensitivity and complementary sensitivity function matrices specified as two weight functions  $W_1(e^{j\omega})$  and  $W_2(e^{j\omega})$ , find a stable controller that satisfy the following relationships for some positive scalar  $\gamma$ .

$$\begin{aligned} \bar{\sigma}\{S(e^{j\omega})\} W_1(e^{j\omega}) &\leq \gamma \\ \bar{\sigma}\{T(e^{j\omega})\} W_3(e^{j\omega}) &\leq \gamma \end{aligned} \quad (24)$$

Here,  $\bar{\sigma}\{G(e^{j\omega})\}$  denotes the maximum singular value of the matrix  $G(z)$  evaluated at  $z = e^{j\omega}$  for  $\omega$  ranging from 0 to  $\pi$ . Roughly speaking, the weight  $W_1(e^{j\omega})$  is specified

for the desired bandwidth at low frequencies and  $W_3(e^{j\omega})$  is specified for the stability robustness for the uncertainty at high frequencies. It is also possible to include another weight function to keep the controller output under an admissible level, but it is omitted here assuming the actuator has sufficient ability to address the given disturbance. The discrete-time controller  $\mathbf{K}_H(z)$  is obtained by solving the  $H_\infty$  mixed sensitivity problem for the plant  $z^{-1}\mathbf{P}_H(z)$  with the following weight functions.

$$W_1(z) = \frac{0.5043z - 4956}{z - 0.9998} \quad (25)$$

$$W_3(z) = \frac{6.499z - 5.853}{z - 0.3471} \quad (26)$$

Figure 14 shows the frequency response of these weight functions.

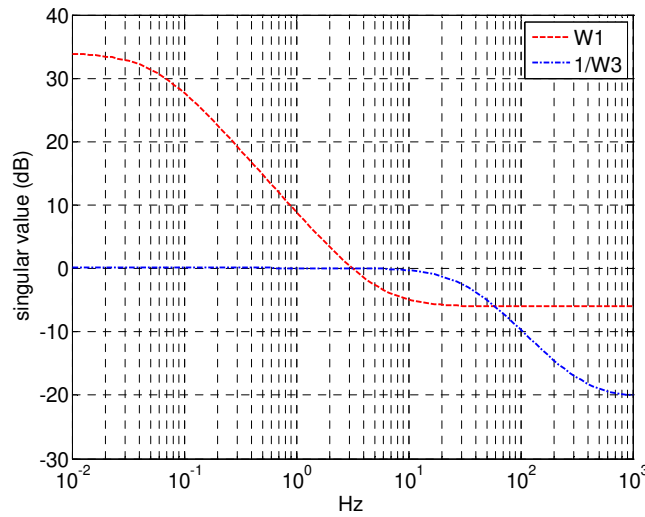


**Figure 14** Frequency responses of the weight functions used for  $H_\infty$  mixed sensitivity loop shaping

Detailed theory and design of  $H_\infty$  controller can be found in many books and literature such as (Zhou and Doyle, 1997). The obtained discrete-time  $H_\infty$  controller  $\mathbf{K}_H(z)$  has 102 input and output channels and 638 states.

The open-loop transfer function matrix  $\mathbf{L}_{Hc}(z)$ , the complementary sensitivity function matrix  $\mathbf{T}_{Hc}(z)$ , and the sensitivity function matrix  $\mathbf{S}_{Hc}(z)$  are written as follows. The feedback loop is stable and the value of  $\gamma$  is 0.9993.

$$\mathbf{L}_{Hc}(z) = z^{-1}\mathbf{P}_H(z)\mathbf{K}_H(z). \quad (27)$$

$$\mathbf{T}_{Hc}(z) = \mathbf{L}_{Hc}(z)[\mathbf{I} + \mathbf{L}_{Hc}(z)]^{-1} \quad (28)$$

$$\mathbf{S}_{Hc}(z) = [\mathbf{I} + \mathbf{L}_{Hc}(z)]^{-1} \quad (29)$$

Figure 15 and Figure 16 show the singular value plots of Equation (28) and (29) in the control space, respectively. The bandwidth of the system is higher than 10Hz and the sensitivity and complementary sensitivity functions appear to be satisfactory. However, the plots show the performance of the controller in the control space, i.e., the performance for the disturbance projected onto the selected basis vectors.

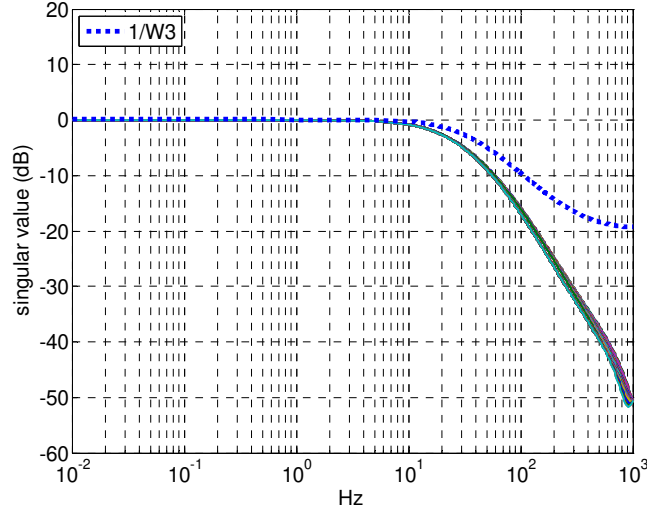


**Figure 15 Singular value plot of the complementary sensitivity function of the  $H_\infty$  controller in control space**

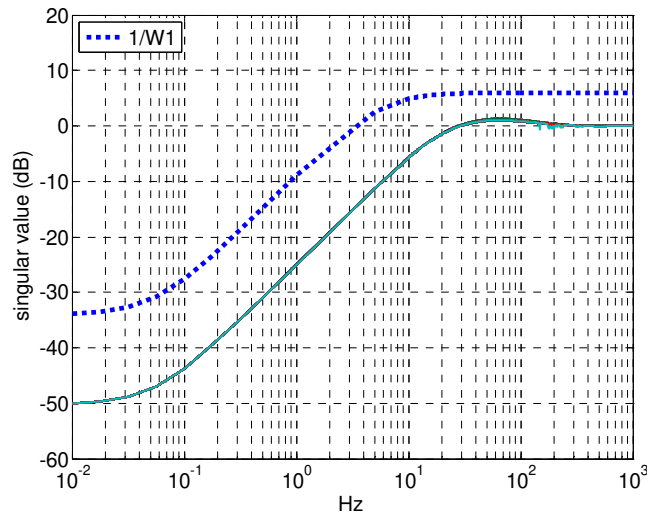


**Figure 16 Singular value plot of the sensitivity function of the  $H_\infty$  controller in control space**

The actual performance of the controller in the sensor space, on the other hand, is different. The transfer functions in the sensor space are written as follows,

$$\mathbf{L}_H(z) = z^{-1}\mathbf{P}(z)\mathbf{C}_H(z) \quad (30)$$



$$\mathbf{T}_H(z) = \mathbf{L}_H(z)[\mathbf{I} + \mathbf{L}_H(z)]^{-1} \quad (31)$$

$$\mathbf{S}_H(z) = [\mathbf{I} + \mathbf{L}_H(z)]^{-1} \quad (32)$$

where

$$\mathbf{C}_H(z) = \mathbf{V}_H \boldsymbol{\Sigma}_H^{-1} \mathbf{K}_H(z) \mathbf{U}_H^T. \quad (33)$$

The controller  $\mathbf{C}_H(z)$  has 720 input and 936 output with 638 states. Figure 17 and Figure 18 show the corresponding singular value plots of Equation (31) and (32), respectively.

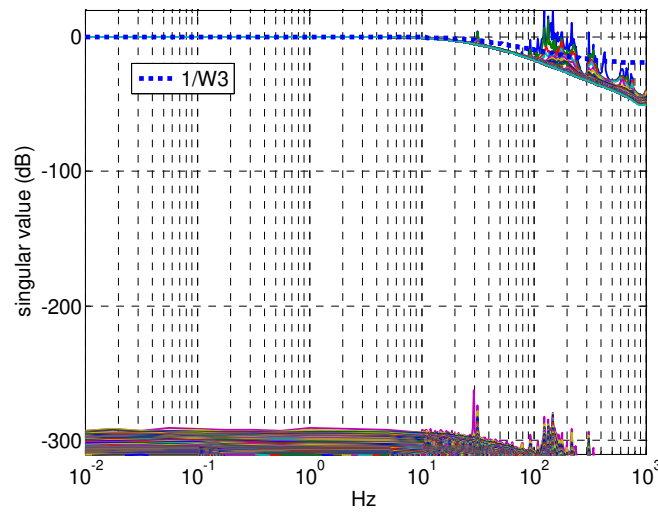


**Figure 17** Singular value plot of the complementary transfer function of the  $H_\infty$  controller in sensor space

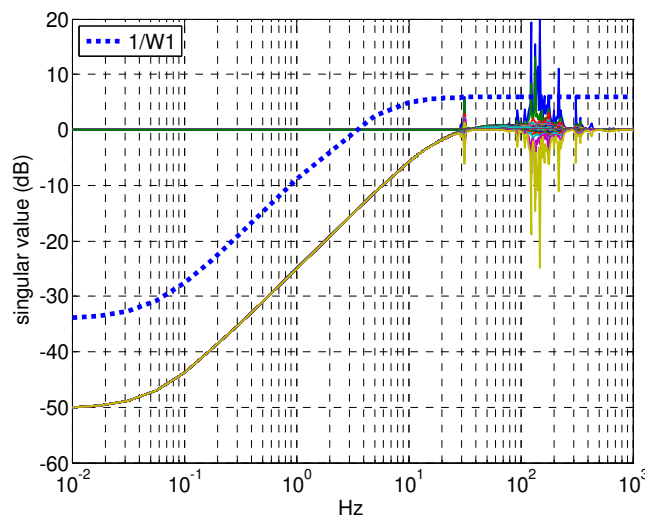


**Figure 18** Singular value plot of the sensitivity function of the  $H_\infty$  controller in sensor space

It can be seen in Figure 17 that while some of the singular values are similar to those found in Figure 15, majority of the singular values are less than -300 dB which is zero with numerical errors. These singular values correspond to the modes that are orthogonal to the selected basis vectors and the disturbance projected onto these modes is ignored by the controller. The singular values for those modes in Figure 18 are therefore 0 dB, which indicates no attenuation of the disturbance.

### III-4 Parallel Controller

One of the controllers proposed in (Looyesen, 2009) combines an  $H_\infty$  controller and a classical SISO controller in parallel and both controllers address the reduced number of modes. In this section, this parallel controller is modified such that the SISO integral controller in Section III-2 addresses the entire sensor space while the  $H_\infty$  controller from Section III-3 addresses only the selected 102 modes. For this controller, the gain of the integral controller needs to be reduced to  $K_i = 0.001$  to make the system stable because of the presence of the  $H_\infty$  controller. The number of states in the parallel controller is 1358. The transfer function matrices are written as follows and Figure 19 and Figure 20 show the corresponding singular value plots.

$$\mathbf{L}_p(z) = z^{-1}\mathbf{P}(z)(\mathbf{C}_H(z) + \mathbf{C}_i(z)) \quad (34)$$

$$\mathbf{T}_p(z) = \mathbf{L}_p(z)[\mathbf{I} + \mathbf{L}_p(z)]^{-1} \quad (35)$$

$$\mathbf{S}_p(z) = [\mathbf{I} + \mathbf{L}_p(z)]^{-1} \quad (36)$$

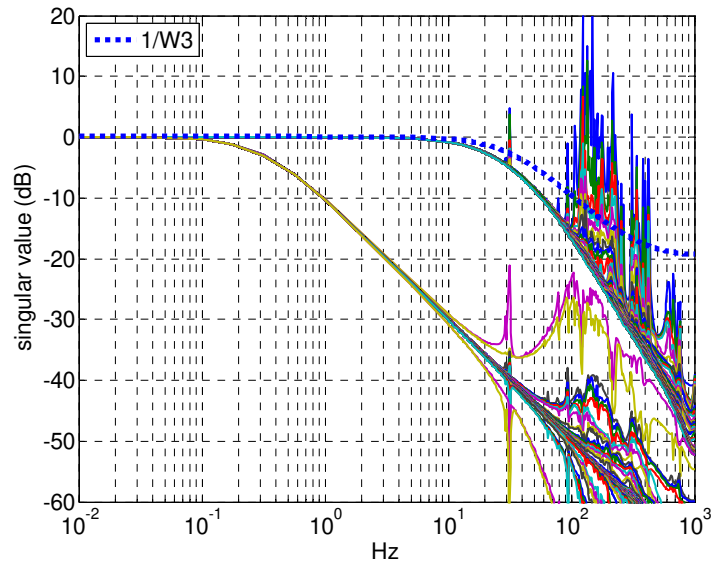


**Figure 19 Singular value plot of the complementary transfer function of the parallel controller in sensor space**

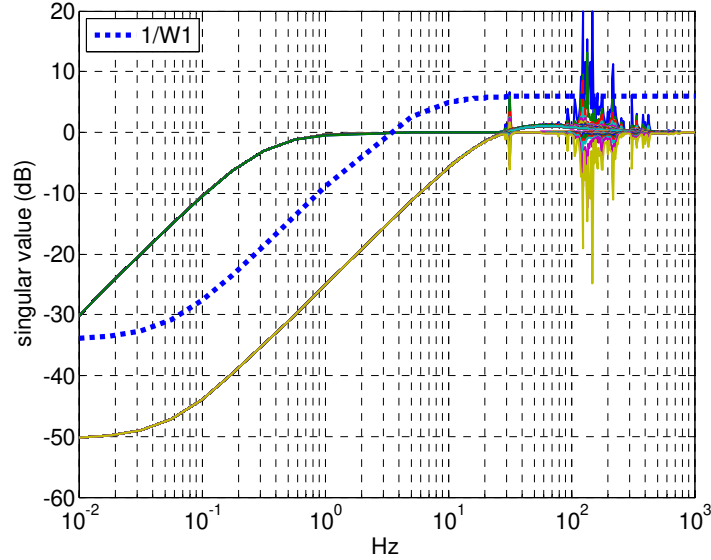


**Figure 20 Singular value plot of the sensitivity function of the parallel controller in sensor space**

The controller now achieves zero steady state error because of the integral controller. But the bandwidth for the modes addressed by the integral controller is even lower than that of the integral controller in Section III-2 because of the reduction of the integrator gain. The bandwidth can be increased by applying a low-pass filter or notch filters as proposed in (Looyesen 2009), but the order of the controller increases significantly because the order of the filter is multiplied by 720 to address all channels. For example, three notch filters or a 6<sup>th</sup> order elliptic filter increases the controller states by 4320, which is not desirable for real-time implementation of the controller.

### III-5 Dynamics Decoupling Control

In this section, the proposed design method to overcome the shortcomings of the previous methods is developed. Consider the statically uncoupled plant in Equation (16) re-written in a state-space form as follows.

$$\begin{aligned} \mathbf{x}(k+1) &= \mathbf{A}_c \mathbf{x}(k) + \mathbf{B}_c \mathbf{u}(k) \\ \mathbf{y}(k) &= \mathbf{C}_c \mathbf{x}(k) + \mathbf{D}_c \mathbf{u}(k) \end{aligned} \quad (37)$$

The plant consists of the following purely dynamic sub-plant

$$\mathbf{G}_c(z) = \mathbf{C}_c (z\mathbf{I} - \mathbf{A}_c)^{-1} \mathbf{B}_c \quad (38)$$

and a constant matrix  $\mathbf{D}_c$  representing the static sub-plant. If the rank of  $\mathbf{D}_c$  is the same as those of  $\mathbf{G}_c(e^{j\omega})$  evaluated from  $\omega = 0$  to  $\omega = \pi$ , then the plant dynamics is fully coupled and the controller cannot avoid having a dimension that is equal or greater than the rank of  $\mathbf{D}_c$  to address all spatial and temporal modes. To reduce the dimension of

the model, it is necessary to ignore some of the modes in such a case and the performance is compromised. However, if the rank of  $\mathbf{G}_c(e^{j\omega})$  at the frequencies of interest is lower than the that of  $\mathbf{D}_c$ , the dimension of the dynamic sub-plant can be reduced by modal decomposition as described below.

Consider the case where  $\mathbf{B}_c$  is a  $k \times n$  matrix and has a rank  $r_b < n$ , and  $\mathbf{D}_c$  has a rank of  $n$ . By applying SVD,  $\mathbf{B}_c$  can be expressed as

$$\mathbf{B}_c = \mathbf{U}_B \boldsymbol{\Sigma}_B \mathbf{V}_B^T = [\mathbf{U}_{B1}, \mathbf{U}_{B2}] \begin{bmatrix} \boldsymbol{\Sigma}_{B1} & \mathbf{0} \\ \mathbf{0} & \mathbf{0} \end{bmatrix} \begin{bmatrix} \mathbf{V}_{B1}^T \\ \mathbf{V}_{B2}^T \end{bmatrix} \quad (39)$$

where  $\mathbf{U}_{B1}$  and  $\mathbf{V}_{B1}$  are the first  $r_b$  vectors of  $\mathbf{U}_B$  and  $\mathbf{V}_B$ , respectively. The diagonal matrix  $\boldsymbol{\Sigma}_{B1}$  consists of the first  $r_b$  non-zero singular values, and  $\mathbf{U}_{B2}$  and  $\mathbf{V}_{B2}$  consist of the rest of the column vectors of  $\mathbf{U}_B$  and  $\mathbf{V}_B$ , respectively, which are associated with zero singular values. Since  $\mathbf{B}_c \mathbf{V}_{B2} = \mathbf{0}$ , the plant can be separated into a dynamic plant and a static plant to be controlled by two different commands as shown below.

$$\mathbf{P}_c(z)(\mathbf{V}_{B1} \mathbf{u}_1 + \mathbf{V}_{B2} \mathbf{u}_2) = \mathbf{P}_1(z) \mathbf{u}_1 + \mathbf{P}_2 \mathbf{u}_2 \quad (40)$$

Here,  $\mathbf{u}_1 \in \mathfrak{R}^{r_b}$  and  $\mathbf{u}_2 \in \mathfrak{R}^{n-r_b}$  and  $\mathbf{P}_1(z)$  is the dynamic plant

$$\begin{aligned} \mathbf{P}_1(z) &= \mathbf{P}_c(z) \mathbf{V}_{B1} = (\mathbf{C}_c(z\mathbf{I} - \mathbf{A}_c)^{-1} \mathbf{B}_c + \mathbf{D}_c) \mathbf{V}_{B1} \\ &= \mathbf{C}_c(z\mathbf{I} - \mathbf{A}_c)^{-1} \mathbf{B}_c \mathbf{V}_{B1} + \mathbf{D}_c \mathbf{V}_{B1} = \mathbf{G}_{c1}(z) \mathbf{V}_{B1} + \mathbf{D}_{c1} \end{aligned} \quad (41)$$

whose input dimension is  $r_b$ , and  $\mathbf{P}_2$  is the static plant

$$\begin{aligned} \mathbf{P}_2 &= \mathbf{P}_c(z) \mathbf{V}_{B2} = (\mathbf{C}_c(z\mathbf{I} - \mathbf{A}_c)^{-1} \mathbf{B}_c + \mathbf{D}_c) \mathbf{V}_{B2} \\ &= \mathbf{C}_c(z\mathbf{I} - \mathbf{A}_c)^{-1} \mathbf{B}_c \mathbf{V}_{B2} + \mathbf{D}_c \mathbf{V}_{B2} = \mathbf{0} + \mathbf{D}_c \mathbf{V}_{B2} = \mathbf{D}_{c2} \end{aligned} \quad (42)$$

whose input dimension is  $n - r_b$ . The direct path of the dynamic and static plants are denoted by  $\mathbf{D}_{c1} = \mathbf{D}_c \mathbf{V}_{B1}$  and  $\mathbf{D}_{c2} = \mathbf{D}_c \mathbf{V}_{B2}$ , respectively. The controllability of the system is not changed by this separation since Equation (40) can be written with  $\mathbf{u} = [\mathbf{u}_1^T, \mathbf{u}_2^T]^T \in \mathfrak{R}^n$  as

$$\mathbf{P}_c(z) \mathbf{V}_B \mathbf{u} = \mathbf{P}_c(z) (\mathbf{V}_{B1} \mathbf{u}_1 + \mathbf{V}_{B2} \mathbf{u}_2), \quad (43)$$

and post-multiplying  $\mathbf{P}_c(z)$  with an orthogonal matrix  $\mathbf{V}_B$  is just a coordinate conversion.

The system represented by the right hand side of Equation (40) has the structure of so-called Dual-Input Single-Output (DISO) system. DISO system can be found in redundant actuator systems such as the dual-stage actuator head positioning system in Hard Disk Drives. A control technique called SDM developed for scalar DISO systems can be extended for the MIMO system given by Equation (40). The SDM realizes a

feedback loop for  $\mathbf{P}_c(z)$  that is equivalent of a series of two separate or "decoupled" feedback loops for  $\mathbf{P}_1(z)$  and  $\mathbf{P}_2$ . Figure 21 shows the structure of the SDM controller, where  $\mathbf{C}_1(z)$  and  $\mathbf{C}_2(z)$  are the controllers addressing  $\mathbf{P}_1(z)$  and  $\mathbf{P}_2$ , respectively, and  $\hat{\mathbf{P}}_2$  is the estimate of the plant  $\mathbf{P}_2$ . The SDM removes the effect of  $\mathbf{C}_2(z)$  from the error observed by  $\mathbf{C}_1(z)$  using the plant estimate  $\hat{\mathbf{P}}_2$ , so that  $\mathbf{C}_1(z)$  works as if  $\mathbf{C}_2(z)$  does not exist. In other words, the feedback loop of  $\mathbf{C}_1(z)$  is decoupled from the feedback loop of  $\mathbf{C}_2(z)$ .

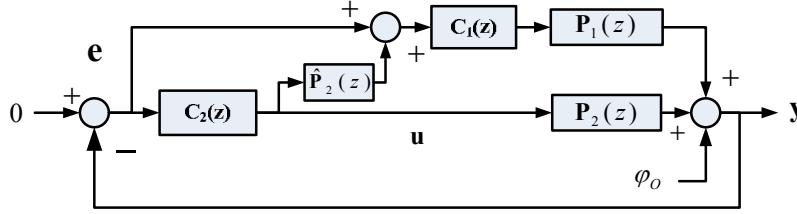


**Figure 21 Diagram of the dynamics decoupling controller**

The benefit of this scheme, referred here as the dynamics decoupling control, is that the controller  $\mathbf{C}_1(z)$  and  $\mathbf{C}_2(z)$  can be designed independently for  $\mathbf{P}_1(z)$  and  $\mathbf{P}_2$ . Significant reduction of the computation can be achieved for a system where the rank of  $\mathbf{P}_1(1)$  is much smaller than that of  $\mathbf{P}_2$ , since a MIMO controller is needed only for the dynamic plant  $\mathbf{P}_1(z)$  and the classical SISO controller described in Section III-2 can be applied for the static plant  $\mathbf{P}_2$  which does not require extensive computation to design. For the plant model considered here, the rank reduction of the dynamic part is caused by the constant B matrix which does not depend on the frequency. As a result, the separation is valid not only for the steady state response but also for the entire frequency of the discrete-time system.

In practice, it makes the controller design easier to further transform  $\mathbf{P}_1(z)$  and  $\mathbf{P}_2$  to different controller spaces by different SVD bases. In the following, detailed development of the dynamics decoupling controller is presented. For  $\mathbf{P}_1(z)$ , the plant in the control space is written as follows.

$$\mathbf{P}_{c1}(z) = \mathbf{U}_1^T \mathbf{P}_1(z) \mathbf{V}_1 \mathbf{\Sigma}_1^{-1} \quad (44)$$

Here,  $\mathbf{U}_1$ ,  $\mathbf{V}_1$ , and  $\mathbf{\Sigma}_1$  are the SVD of  $\mathbf{P}_1(1)$ , i.e.,  $\mathbf{P}_1(1) = \mathbf{U}_1 \mathbf{\Sigma}_1 \mathbf{V}_1^T$ , where the number of the columns of  $\mathbf{U}_1$ ,  $\mathbf{V}_1$ , and the diagonal matrix  $\mathbf{\Sigma}_1$  are the same as the rank of  $\mathbf{P}_1(1)$ . A MIMO controller  $\mathbf{C}_{H1}(z)$  is designed for  $z^{-1} \mathbf{P}_{c1}(z)$  by the  $H_\infty$  loop shaping described in Section III-3 with the same weights in Equation (25) and (26). The controller  $\mathbf{C}_{H1}(z)$  is then converted back to the original control space as follows.

$$\mathbf{C}_1(z) = \mathbf{V}_1 \mathbf{\Sigma}_1^{-1} [\mathbf{C}_{H1}(z)] \mathbf{U}_1^T \quad (45)$$

The controller for plant  $\mathbf{P}_2$  is obtained in the same manner. The plant  $\mathbf{P}_2$  is transformed to another control space by

$$\mathbf{P}_{c2} = \mathbf{U}_2^T \mathbf{P}_2 \mathbf{V}_2 \mathbf{\Sigma}_2^{-1}, \quad (46)$$

where matrices  $\mathbf{U}_2$ ,  $\mathbf{V}_2$ , and  $\mathbf{\Sigma}_2$  are the SVD of  $\mathbf{P}_2 = \mathbf{U}_2 \mathbf{\Sigma}_2 \mathbf{V}_2^T$  whose dimensions are minimized to the rank of matrix  $\mathbf{P}_2$ . Since  $\mathbf{P}_2$  is a matrix without any dynamics,  $\mathbf{P}_{c2}$  is completely uncoupled, i.e., an identity matrix for the entire frequency range. An integral controller  $\mathbf{C}_{i2}(z)$  can be obtained by expanding an SISO integral controller by an identity matrix with an appropriate dimension.

$$\mathbf{C}_{i2}(z) = K_{i2} \frac{z}{z-1} \mathbf{I}. \quad (47)$$

The design of  $\mathbf{C}_{i2}(z)$  is an SISO problem and a stable gain  $K_{i2}$  can easily be determined. Since the dynamics in the loop is only the unit step delay for the plant considered here, the gain of the controller can be chosen sufficiently high for a reasonable bandwidth without making the feedback loop unstable. The upper limit of the gain is most likely set by the level of the measurement noise than the stability bound. The controller  $\mathbf{C}_2(z)$  in the original control space is obtained as follows.

$$\mathbf{C}_2(z) = \mathbf{V}_2 \mathbf{\Sigma}_2^{-1} \mathbf{C}_{i2}(z) \mathbf{U}_2^T \quad (48)$$

Finally, the complete dynamics decoupling controller is obtained for  $\mathbf{P}_c(z)$  by combining  $\mathbf{C}_1(z)$  and  $\mathbf{C}_2(z)$  through the SDM as

$$\mathbf{C}_d(z) = \mathbf{V}_{B1} \mathbf{C}_1(z) (\mathbf{I} + z^{-1} \hat{\mathbf{P}}_2 \mathbf{C}_2(z)) + \mathbf{V}_{B2} \mathbf{C}_2(z). \quad (49)$$

The controller to be applied in the actual system can be obtained as follows

$$\mathbf{C}_{dAO}(z) = \mathbf{G}_{AO} \mathbf{C}_d(z) \mathbf{F}_{AO}, \quad (50)$$

where  $\mathbf{F}_{AO} = \mathbf{U}_{AO}^T$  and  $\mathbf{G}_{AO} = \mathbf{V}_{AO} \mathbf{\Sigma}_{AO}^{-1}$ .

The stability of this controller can be verified as follows. The relationship from the output disturbance  $\varphi_O$  to the error  $\mathbf{e}$  can be written as

$$\begin{aligned} \mathbf{e} &= -z^{-1} \mathbf{P} \mathbf{C}_{dAO} \mathbf{e} - \varphi_O \\ &= -z^{-1} \mathbf{P} \mathbf{G}_{AO} \mathbf{C}_d \mathbf{F}_{AO} \mathbf{e} - \varphi_O \\ &= -z^{-1} \mathbf{P} \mathbf{G}_{AO} (\mathbf{V}_{B1} \mathbf{C}_1 + \mathbf{V}_{B1} \mathbf{C}_1 (z^{-1} \hat{\mathbf{P}}_2 \mathbf{C}_2) + \mathbf{V}_{B2} \mathbf{C}_2) \mathbf{F}_{AO} \mathbf{e} - \varphi_O, \end{aligned} \quad (51)$$

where the step delay is introduced and  $(z)$  is omitted for brevity. Pre-multiplying  $\mathbf{F}_{AO}$  to both sides and moving the controller term to the left hand side yields

$$\begin{aligned}
& \mathbf{F}_{AO} \mathbf{e} + z^{-1} \mathbf{F}_{AO} \mathbf{P} \mathbf{G}_{AO} \left[ \mathbf{V}_{B1} \mathbf{C}_1 (\mathbf{I} + z^{-1} \hat{\mathbf{P}}_2 \mathbf{C}_2) + \mathbf{V}_{B2} \mathbf{C}_2 \right] \mathbf{F}_{AO} \mathbf{e} \\
&= \left\{ \mathbf{I} + z^{-1} \mathbf{P}_c \left[ \mathbf{V}_{B1} \mathbf{C}_1 (\mathbf{I} + z^{-1} \hat{\mathbf{P}}_2 \mathbf{C}_2) + \mathbf{V}_{B2} \mathbf{C}_2 \right] \right\} \mathbf{F}_{AO} \mathbf{e} \\
&= \left[ \mathbf{I} + z^{-1} \mathbf{P}_1 \mathbf{C}_1 (\mathbf{I} + z^{-1} \hat{\mathbf{P}}_2 \mathbf{C}_2) + z^{-1} \mathbf{P}_2 \mathbf{C}_2 \right] \mathbf{F}_{AO} \mathbf{e} \\
&= -\mathbf{F}_{AO} \varphi_O
\end{aligned} \tag{52}$$

If  $\hat{\mathbf{P}}_2 = \mathbf{P}_2$ , then

$$\begin{aligned}
& \left[ \mathbf{I} + z^{-1} \mathbf{P}_1 \mathbf{C}_1 + (z^{-1} \mathbf{P}_1 \mathbf{C}_1 + \mathbf{I}) z^{-1} \mathbf{P}_2 \mathbf{C}_2 \right] \mathbf{F}_{AO} \mathbf{e} = -\mathbf{F}_{AO} \varphi_O \\
& \left( \mathbf{I} + z^{-1} \mathbf{P}_1 \mathbf{C}_1 \right) \left( \mathbf{I} + z^{-1} \mathbf{P}_2 \mathbf{C}_2 \right) \mathbf{F}_{AO} \mathbf{e} = -\mathbf{F}_{AO} \varphi_O \\
& \mathbf{F}_{AO} \mathbf{e} = -\left( \mathbf{I} + z^{-1} \mathbf{P}_2 \mathbf{C}_2 \right)^{-1} \left( \mathbf{I} + z^{-1} \mathbf{P}_1 \mathbf{C}_1 \right)^{-1} \mathbf{F}_{AO} \varphi_O
\end{aligned} \tag{53}$$

For a plant whose spatial modes can be fully controlled such as the plant considered here, the matrix  $\mathbf{F}_{AO}$  is an orthogonal diagonal matrix and  $\mathbf{F}_{AO} \mathbf{F}_{AO}^T = \mathbf{F}_{AO}^T \mathbf{F}_{AO} = \mathbf{I}$ . Therefore, Equation (53) can be written as

$$\mathbf{e} = -\mathbf{F}_{AO}^T \left( \mathbf{I} + z^{-1} \mathbf{P}_2 \mathbf{C}_2 \right)^{-1} \left( \mathbf{I} + z^{-1} \mathbf{P}_1 \mathbf{C}_1 \right)^{-1} \mathbf{F}_{AO} \varphi_O \tag{54}$$

and the sensitivity function is obtained as

$$\mathbf{S} = \mathbf{F}_{AO}^T \left( \mathbf{I} + z^{-1} \mathbf{P}_2 \mathbf{C}_2 \right)^{-1} \left( \mathbf{I} + z^{-1} \mathbf{P}_1 \mathbf{C}_1 \right)^{-1} \mathbf{F}_{AO} . \tag{55}$$

Equation (55) shows that the feedback system is stable if the sensitivity functions of the two feedback loops for  $z^{-1} \mathbf{P}_1(z) \mathbf{C}_1(z)$  and  $z^{-1} \mathbf{P}_2 \mathbf{C}_2(z)$  are both stable, since  $\mathbf{F}_{AO}$  and  $\mathbf{F}_{AO}^T$  perform only coordinate conversion.

For the given plant, the rank of  $\mathbf{P}_1(1)$  and  $\mathbf{P}_2$  are 102 and 618, respectively. The number of input/output channels of  $\mathbf{P}_{c1}(z)$  is 102 and the number of states is 332. The dimension of  $\mathbf{P}_{c2}$  is 618×618. The controller  $\mathbf{C}_{H1}(z)$  is designed by the  $H_\infty$  loop shaping with the weights in Equation (25) and (26), and the integral controller presented in Section III-2 is used for  $\mathbf{C}_{i2}(z)$  with  $K_i = 0.06$ . The states of the controllers  $\mathbf{C}_1(z)$  and  $\mathbf{C}_2(z)$  are 638 and 618, respectively, and the states for the decoupling-path term are also 618. The total number of states is therefore 1874 for  $\mathbf{C}_d(z)$ . The value of  $\gamma$  in the computation of  $\mathbf{C}_{H1}(z)$  is 0.9975. For  $\mathbf{C}_1(z)$  and  $\mathbf{C}_2(z)$  designed here, the two sensitivity functions in Equation (55) are stable, and therefore the whole feedback system is also stable.

The open-loop transfer function  $\mathbf{L}_d(z)$ , the complementary sensitivity function  $\mathbf{T}_d(z)$ , sensitivity function  $\mathbf{S}_d(z)$  in the sensor space are written as follows.

$$\mathbf{L}_d(z) = z^{-1} \mathbf{P}(z) \mathbf{C}_{dAO}(z) \tag{56}$$

$$\mathbf{S}_d(z) = \left( \mathbf{I} + z^{-1} \mathbf{P}(z) \mathbf{G}_{AO} \mathbf{V}_{b2} \mathbf{C}_2(z) \mathbf{F}_{AO} \right)^{-1} \left( \mathbf{I} + z^{-1} \mathbf{P}(z) \mathbf{G}_{AO} \mathbf{V}_{b1} \mathbf{C}_1(z) \mathbf{F}_{AO} \right)^{-1} \tag{57}$$

$$\mathbf{T}_d(z) = \mathbf{I} - \mathbf{S}_d(z) \quad (58)$$

The different expression of  $\mathbf{S}_d(z)$  in Equation (57) can be obtained using Equations (16), (42), (51), and the orthogonality property of  $\mathbf{F}_{AO}$ . Figure 22, Figure 23, and Figure 24 show the singular values of  $\mathbf{L}_d(z)$ ,  $\mathbf{T}_d(z)$ , and  $\mathbf{S}_d(z)$ , respectively.

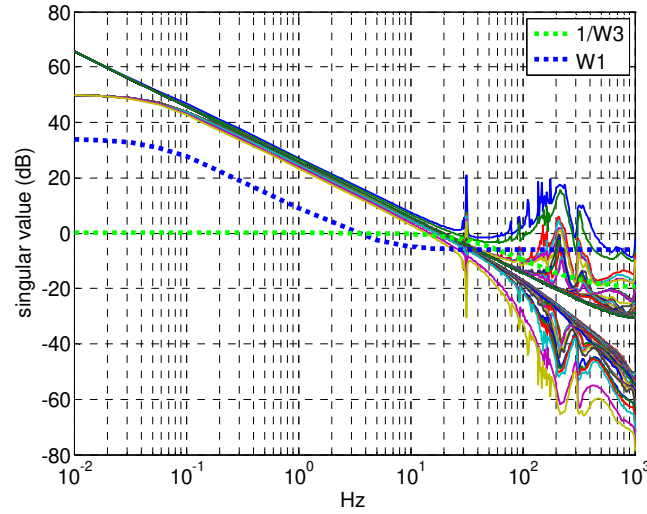


**Figure 22 Singular value plot of the open-loop function of the dynamics decoupling controller in sensor space**

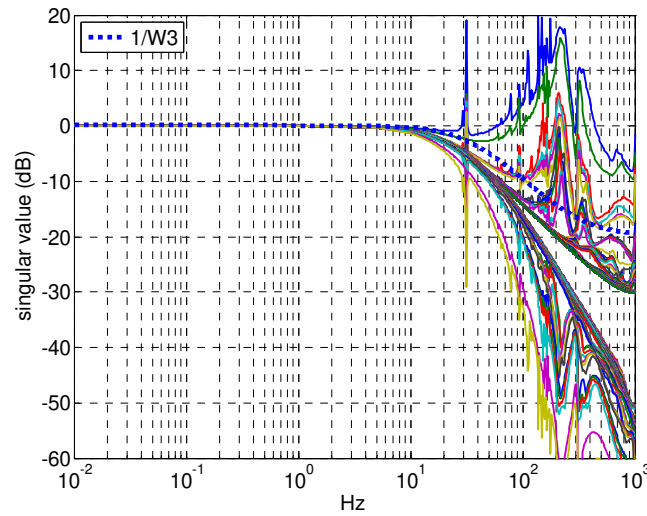


**Figure 23 Singular value plot of the complementary sensitivity function of the dynamics decoupling controller in sensor space**



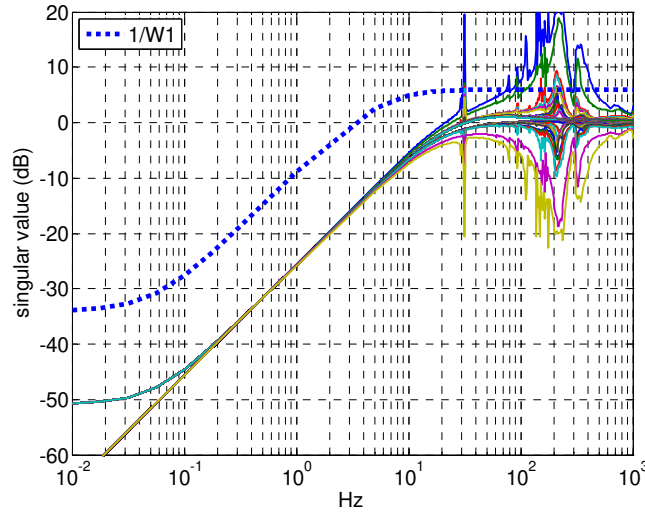


**Figure 24 Singular value plot of the sensitivity function of the dynamics decoupling controller in sensor space**

From Figure 23, it can be seen that the bandwidths of all modes are above 10Hz. There are resonances whose magnitudes are close to 20dB, but only two modes have such significant gains and the rest of the modes are below 10dB for the entire frequency range. Those resonances can be alleviated by modifying the weight functions, or by reducing the loop gain. In either case, it will result in a lower bandwidth.

#### IV SIMULATION RESULT

Numerical simulation was conducted for the controllers presented in the previous sections, namely, the integral controller in Section III-2,  $H_\infty$  controller in Section III-3, the parallel controller in Section III-4, and the proposed dynamics decoupling controller developed in Section III-5. Figure 25 shows the block diagram of the system used in the simulation.

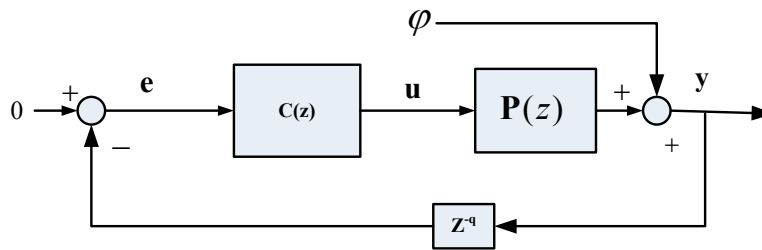


**Figure 25 System model of the simulation**

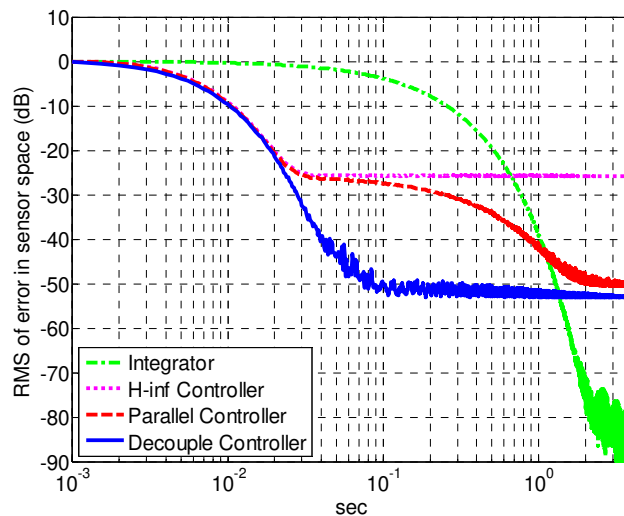
The step delay  $q$  is 1. The performances of the controllers were first evaluated for two kinds of step input disturbance  $\varphi$  applied as an output disturbance. The first disturbance, referred here as disturbance 1, is the disturbance used to sort the SVD modes for the design of the  $H_\infty$  controller and the parallel controller. The second disturbance, referred here as disturbance 2, has random values for each channel. Both disturbances are normalized, i.e., the Root Mean Square (RMS) of the magnitude of all

channels is unity. Table 1 shows the controller parameters and number of modes addressed by each controller.

**Table 1 Parameters of the controllers and addressed modes**

Controller	Integrator Gain	Controlled Spatial Modes
Integral Controller	$K_i = 0.0022$	720
$H_\infty$ Controller	-	102
Parallel Controller ( $H_\infty + \text{Integral}$ )	$K_i = 0.001$	720 (Integral) 102 ( $H_\infty$ )
Dynamics Decoupling Controller	$K_{i2} = 0.06$	618 (Integral) 102 ( $H_\infty$ )

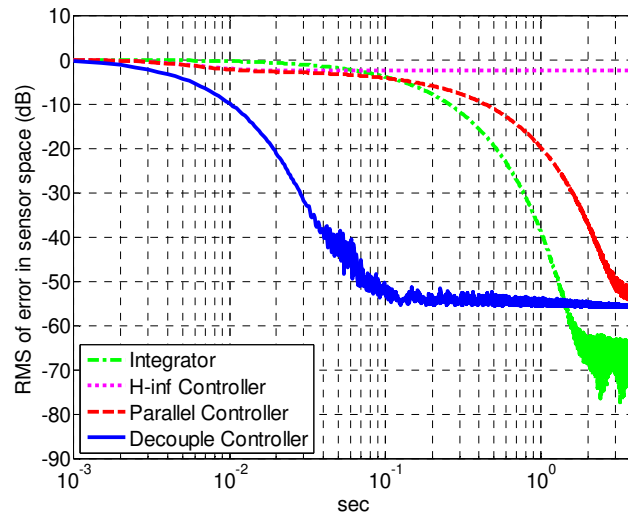
Figure 26 shows the RMS of the errors in the sensor space for disturbance 1. As expected, the convergence of the integrator is much slower than the other controllers. The  $H_\infty$  controller, the parallel controller, and the proposed controller converge at similar rates until the attenuation of the  $H_\infty$  controller saturates due to the fact that the controller addresses only 102 spatial modes. The convergence of the parallel controller also slows down at the similar point because it uses the same  $H_\infty$  controller and further attenuation is the result of much slower integral controller working in parallel. The proposed controller maintains the fast convergence rate until it reaches the error floor determined by the weight function specified in the design process.



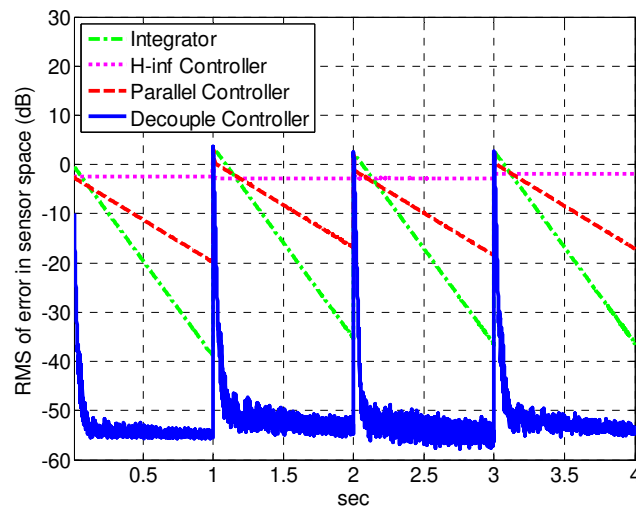
**Figure 26 RMS of the sensor space error of the integral, parallel,  $H_\infty$ , and dynamics decoupling controllers for disturbance 1**

Figure 27 shows the RMS of the errors for disturbance 2. In contrast to the case shown in Figure 26 where significant part of the disturbance component was attenuated by the  $H_\infty$  controller, the error reduction is now significantly reduced because the energy of disturbance 2 is no longer concentrated on the modes addressed by the  $H_\infty$  controller. The parallel controller has an integral controller that addresses all modes, but

because of the bandwidth of the integral part that is much lower than that of the  $H_\infty$  counterpart, the convergence is very slow. The proposed controller, on the other hand, is not affected by the change of the spatial characteristics of the disturbance. The convergence rate of the integral controller is also not affected, but it is much slower than the proposed method as in the previous case. Figure 28 shows the RMS of the error when the direction of the disturbance vector was randomly changed at every one second. The RMS of all disturbance vectors are normalized. This disturbance profile can be considered as slewing maneuvers of the telescope to acquire new targets. The result demonstrates that the convergence of the proposed method is consistently faster than those of the compared controllers regardless of the changes in the spatial characteristics of the disturbance.



**Figure 27 RMS of the sensor space error of the integral, parallel,  $H_\infty$ , and dynamics decoupling controllers for disturbance 2**



**Figure 28 RMS of the sensor space error of the integral, parallel,  $H_\infty$ , and dynamics decoupling controllers for random step output disturbance**

## V CONCLUSION

A practical control design method has been proposed for a class of large SMT AO systems, where the dimension of the system representing the whole plant is too large to apply a standard MIMO controller design method but the dimension of the subsystem representing the truly dynamic part of the plant is much smaller and tractable. The proposed method separates the plant into the dynamic path and the static path through a modal decomposition of the B matrix of the plant state-space model and designs a controller for each path separately. Since the proposed method designs the MIMO controller only for the dynamic path, the computational burden is significantly reduced. The static path can be addressed by a classical SISO controller with the conventional modal decomposition technique which does not require extensive computation.

The controller designed for each path is then combined using the SDM so that the resulting feedback loop is represented by a series of two feedback loops addressing the dynamic and the static paths separately. The stability of the controller is assured as long as the feedback loops for the dynamic and static paths are stable and the plant estimation for the decoupling path is accurate. It should be noted that the separation of the dynamic and static paths is done by the property of the B matrix which does not depend on the frequency. Therefore, the separation is valid through the entire frequency range and not only for the steady-state approximation used in the design process.

To demonstrate the effectiveness of the proposed method, a dynamics decoupling controller was designed for an SMT model. A MIMO controller for the dynamic path was developed by the  $H_\infty$  loop shaping technique and an SISO integral controller was used for the static path. The obtained controller achieved a bandwidth higher than the desired 10 Hz and the time-domain simulation results showed faster convergence of the controller than other controllers compared. A drawback of the proposed method is that it requires a model of the plant and the modelling error affects both stability and performance of the controller. Further investigation is necessary to evaluate the robustness of the proposed method with respect to the modelling error.

## ACKNOWLEDGEMENT

This research was conducted while the first author held the National Research Council Research Associateship at the Naval Postgraduate School.

## REFERENCES

- Allen, M. R. (2007) 'Wavefront Control for Space Telescope Applications Using Adaptive Optics', M.S. Thesis, Naval Postgraduate School (U.S.), Department of Mechanical and Astronautical Engineering.
- Allen, M. R., Kim, J. J. and Agrawal, B. (2008) 'Control of a Deformable Mirror Subject to Structural Disturbance', *SPIE Defense and Security Symposium*.
- Burtz, D. C. (2009) 'Fine Surface Control of Flexible Space Mirrors Using Adaptive Optics and Robust Control', Ph.D. Dissertation, Naval Postgraduate School (U.S.), Department of Mechanical and Astronautical Engineering.

- Frazier, B. W. (2003) 'Closed-loop results of a compact high-speed adaptive optics system with  $H^\infty$ ', *Proceedings of SPIE*, 5169, pp. 37-42.
- Gavel, D. T. and Wiberg, D. (2003) 'Toward Strehl-optimizing adaptive optics controllers', *Proceedings of SPIE*, 4839(1), pp. 890-901.
- Gibson, J. S., Chang, C.-C. and Chen, N. (2001) 'Adaptive optics with a new modal decomposition of actuator and sensor spaces', *Proceedings of the 2001 American Control Conference*, 6, pp. 4619-4625.
- Hampton, P. J., Agathoklis, P., Conan, R. and Bradley, C. (2010) 'Closed-loop control of a woofer-tweeter adaptive optics system using wavelet-based phase reconstruction', *Journal of the Optical Society of America A*, 27(11), p. A145-A156.
- Kun Li, Kosmatopoulos, E. B., Ioannou, P. A. and Ryaciotaki-Boussalis, H. (2000) 'Large segmented telescopes', *IEEE Control Systems*, 20(5), pp. 59- 72.
- Liu, Y.-T. and Gibson, J. S. (2007) 'Adaptive control in adaptive optics for directed-energy systems', *Optical Engineering*, 46(4), p. 046601.
- Looyesen, M. W. (2009) 'Combined Integral and Robust Control of the Segmented Mirror Telescope', M.S. Thesis, Naval Postgraduate School (U.S.), Department of Mechanical and Astronautical Engineering.
- Monirabbasi, S. and Gibson, J. S. (2010) 'Adaptive control in an adaptive optics experiment', *Journal of the Optical Society of America A*, 27(11), p. A84-A96.
- Mori, K., Munemoto, T., Otsuki, H., Yamaguchi, Y. and Akagi, K. (1991) 'A dual-stage magnetic disk drive actuator using a piezoelectric device for a high track density', *IEEE Transactions on Magnetics*, 27(6), pp. 5298-5300.
- Nagashima, M. and Agrawal, B. (2011) 'Application of complex-valued FXLMS adaptive filter to Fourier basis control of adaptive optics', *Proceedings of the 2011 American Control Conference*, pp. 2939-2944.
- Petit, C., Conan, J. -M, Kulcsár, C., Raynaud, H. -F, et al. (2006) 'First laboratory demonstration of closed-loop Kalman based optimal control for vibration filtering and simplified MCAO', *Proceedings of SPIE*, 6272(1), p. 62721T-62721T-12.
- Poyneer, L. A., Macintosh, B. A. and Véran, J.-P. (2007) 'Fourier transform wavefront control with adaptive prediction of the atmosphere', *Journal of the Optical Society of America. A, Optics, image science, and vision*, 24(9), pp. 2645-60.
- Rhoadarmer, T. A., Klein, L. M., Gibson, J. S., Chen, N. and Liu, Y.-T. (2006) 'Adaptive control and filtering for closed-loop adaptive-optical wavefront reconstruction', *Proceedings of SPIE*, 6306, p. 63060E.
- Roux, B. Le, Conan, Jean-Marc, Kulcsár, Caroline, Raynaud, Henri-François, et al. (2004) 'Optimal control law for classical and multiconjugate adaptive optics.',

*Journal of the Optical Society of America. A, Optics, image science, and vision*, 21(7), pp. 1261-76.

Tyson, R. (2010) *Principles of Adaptive Optics, Third Edition*, 3rd ed. CRC Press.

Tyson, R. K. and Frazier, B. W. (2004) *Field Guide to Adaptive Optics*, SPIE Publications.

Whorton, M. S. (2003) 'Modern control for the secondary mirror of a Giant Segmented Mirror Telescope', *Proceedings of SPIE*, 4840, pp. 140-150.

Zhou, K. and Doyle, J. C. (1997) *Essentials of Robust Control*, 1st ed. NJ, Prentice Hall.